Journal of Civil Engineering and Construction 2022;11(4):189-209
https://doi.org/10.32732/jcec.2022.11.4.189

Response of Wave Dissipating Blocks Composing a Detached Breakwater to Waves with Various Periods

Taro Kakinuma

Graduate School of Science and Engineering, Kagoshima University, Kagoshima 890-0065, Japan
E-mail: taro@oce.kagoshima-u.ac.jp

Received: 16 May 2022; Accepted: 2 August 2022; Available online: 10 September 2022

Abstract: We discuss the response of the wave dissipating blocks composing a detached breakwater to the waves with various periods, based on both the experimental and numerical results. First, in the hydraulic experiments, the number of the blocks fallen by the irregular waves was the largest when the still water level is moderate, namely the HWL. When the large and long wave is incident, the overflow that lasted for a long time fell many blocks at the back of the breakwater. When the irregular waves, long wave, and irregular waves are continuously incident in this order, the first irregular wave train shifted several blocks, and the subsequent long wave dropped these shifted blocks, displacing the blocks around them, whereafter the second irregular wave train dropped many of the displaced blocks. Second, in the vertically two-dimensional calculations, when the long wave struck the breakwater, a large-scale vortex was created near the seabed in front of the breakwater and remained during the pushing wave. The overflow due to the long wave generated negative wave pressure at the top behind the breakwater. Based on both the numerical and experimental results behind the breakwater, when a large positive wave pressure is generated after a negative wave pressure that is not large in absolute value, the number of fallen blocks will reduce. When large and short waves cause overtopping, and negative wave pressure frequently appears behind a breakwater, the blocks at the back of the breakwater can gradually shift, loosening their engagement.
Keywords: Wave dissipating block; Detached breakwater; Irregular waves; Long wave; Permeable breakwater.

1. Introduction

Taking measures against sandy beach erosion is an important role for civil engineers, especially when the beach is often exposed to strong waves and currents. One of the typical methods for erosion control is to install a detached breakwater, which is a coastal structure located around 100 m offshore and usually constructed parallel to the shoreline. A detached breakwater has two functions: to attenuate waves and to deposit sediments behind the breakwater. A block mound detached breakwater is generally easier and at lower cost to construct than other types of detached breakwaters such as caissons, because the main body of a block mound detached breakwater is built by stacking already created wave dissipating blocks. Moreover, the stacked blocks themselves are expected to weaken the force of rushing waves, depending on the block characteristics including shape and density.

However, when violent waves strike a block mound detached breakwater, the wave dissipating blocks will slide down, allowing the high waves and rapid flows to invade behind the breakwater. If large waves continue to be incident, the blocks may slip further and the crevasses may expand, causing the breakwater to gradually lose its functions. Therefore, it is necessary to consider what makes the blocks slip, especially when constructing low-top block mound breakwaters, where “low-top” means that the crown is low and overflows can occur under certain conditions.

The vulnerability of various types of low-top and submerged block/rubble mound breakwaters to wind waves has been investigated in many studies. For example, the field surveys were conducted by e.g. [1, 2] on disaster situations. The hydraulic experiments were also carried out by e.g. [3–5], and the large-scale experiments were performed by [6] to investigate the damage to the armor layer of rubble mound breakwaters due to wave groups, the effect of which were suggested by [7]. Moreover, as will be described later, numerical calculations are useful, and various numerical models without fixed grids have also been developed to examine the functions of block mound breakwaters: the Lagrangian models were applied by [8–10], whereas a mesh adaptation method was used by [11] to reproduce the detailed flow around a deformed block. The damage in rubble mound breakwaters has been summarized based on historical and future perspectives by [12, 13].

In the actual design and maintenance of block/rubble mound breakwaters, the following concepts have been considered. The estimation method for the wave height transmission coefficient was proposed by [14, 15]. The strikes of breaking waves on wave dissipating blocks were investigated by [16, 17]. The optimal design algorithms

for rubble mound structures with incident irregular waves were developed by [18], and the criteria and methods for designing detached breakwaters were considered by [19–21]. The damage assessment methods have also been developed by [22, 23]. The performance design [24] will also become more important for detached breakwaters.

Recently, the 2011 Great East Japan Earthquake revealed the fragility of breakwaters to incident long-period waves [e.g. 25], so breakwaters resilient to external forces exceeding the design level have been investigated. The vulnerability of breakwaters to tsunamis were examined based on both the hydraulic experiments [e.g. 26–30] and numerical simulations. Regarding the latter, the Eulerian methods were applied by e.g. [31, 32] to reproduce the wave and current fields around breakwaters. The Lagrangian models were also applied by [33–35] to study the movements of the armor blocks, huge boulders, and wave dissipating blocks, respectively. Moreover, the practical consideration was advanced by [36–38] for the shape of detached breakwaters, the structural ingenuity for cover blocks, and the stability formula for armor units, respectively.

Based on these results for tsunamis, the long-period components of wind waves, such as swells generated by a storm, are also presumed to pose a threat to block mound breakwaters. For example, the effect of the long-period components of wind waves on coastal structures was suggested by [39], and the reef-zone disaster due to the long-period waves that were bore-like surf beats was investigated by [40]. In Japan, the coastal structures at the Pacific and Kyushu coasts are frequently damaged by swells [41]. Moreover, in 2008, the “roundabout waves” caused great damage to the coast facing the Sea of Japan in Toyama Prefecture. Roundabout waves are long-period waves mainly in winter: when a low atmospheric pressure system stagnates in the eastern part of the Sea of Japan, a storm blows from the north and high waves occur; these high waves propagate as swells to the south and reach Toyama Bay in half a day to a day. Therefore, it is necessary to consider the cases in which short and long waves are continuous.

In the present paper, we discuss the response of the wave dissipating blocks composing a low-top detached breakwater to wind waves with various periods. We performed both the hydraulic experiments and numerical calculations, with different still water levels, incident wave heights, and block arrangement densities. We first conducted hydraulic experiments with incident irregular waves and examined both the block falling and wave transmission. The still water level was a highest high water level (HHWL), a mean monthly-highest water level, namely a high water level (HWL), and a mean water level (MWL), to study the effect of the still water level on the damage of the low-top block mound detached breakwaters.

In the hydraulic experiments, we also generated a long-period wave with a wave period of approximately 30 s to 70 s on the field scale, such as swells due to strong winds, harbor oscillations, and meteotsunamis caused by atmospheric pressure waves [e.g. 42]. The long-period wave was incident alone or in succession with irregular waves.

Second, based on the results obtained from these hydraulic experiments, we performed vertically two-dimensional numerical calculations. Although several Lagrangian methods have also come to be used for the interaction of waves with breakwaters as mentioned above, we assumed that the blocks were fixed and obtained both the wave pressure distributions and velocity vectors around a detached permeable breakwater, using an Eulerian method, to determine how the still water level and large-scale vortex contributed to cause the block sliding. In this study, the scale of the numerical calculations was the same as that of the hydraulic experiments to understand the experimental results, although using both experiments with a small scale and calculations without scale effects is effective to design breakwaters, as recommended by [43].

2. Experimental setup and conditions

2.1 Experimental setup

Figure 1 illustrates the hydraulic flume with a length of 30.0 m, a width of 1.0 m, and a height of 1.5 m. The flume floor consists of 7 floorboards with gradients of 0.0, 1/12, 1/20, 1/30, 1/20, 1/60, and 0.0 from offshore to onshore. The positive direction of the z-axis is vertically upward, and z is 0.0 m at the most offshore horizontal floorboard. The x- and y-axes are horizontal, where the positive direction of the x-axis is toward the shore and the direction of the y-axis is parallel to the shoreline.

The detached breakwater drawn in Figure 1 was built using the wave dissipating block models, which were stacked in three layers, as depicted in Figure 2. The crown height H_c, crown width, and bottom width of the assembled breakwater were 0.16 m, 0.19 m, and 0.26 m, respectively. Below the breakwater, gravels were laid on the floorboards to make a foundation with a length of 1.5 m in the onshore x-axis direction.

Depicted in Figure 3 is one of the wave dissipating block models, which were made of concrete with a weight of 0.19 N. The length scale of the model is 1/43. The lengths indicated in Figure 3 are listed in Table 1, with the corresponding lengths of a prototype. The block shape looks like a combination of three pillars, where one pillar is sandwiched between two pillars rotated at an angle of 90°.

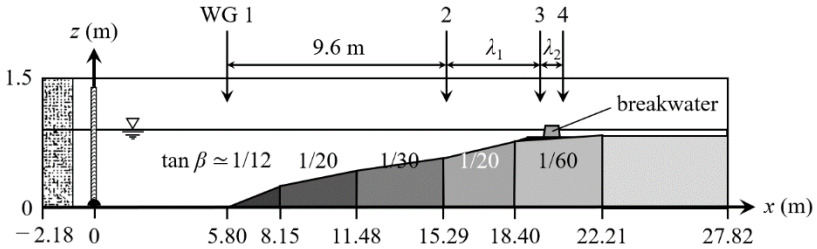

Figure 1. A sketch of the wave flume, where tan β is floorboard gradient. The flap-type wave generating paddle was located at the origin of the x-axis. Four wave gages, namely WGs 1–4, were installed, where the distances λ_1 and λ_2 were 4.1 m and 0.7 m, respectively, when a long wave is incident, whereas 4.0 m and 1.0 m, respectively, in the other cases.

Figure 2. A photograph of a detached breakwater built by stacking the wave dissipating block models in three layers. In each row along the onshore x-axis direction, six, five, and four blocks were arranged in the bottom, middle, and top layers, respectively. In each row along the y-axis direction, 15 blocks were arranged.

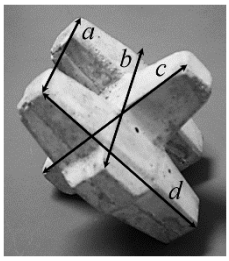

Figure 3. A photograph of one of the wave dissipating block models with a length scale of 1/43. The lengths a, b, c, and d are listed in Table 1.

Table 1. The lengths indicated in Figure 3 for the wave dissipating block model with a length scale of 1/43. The corresponding lengths of the prototype are also described.

	Model Length (m)	Prototype Length (m)
a	0.056	2.4
b	0.072	3.1
c	0.072	3.1
d	0.070	3.0

The model blocks were stacked with the following two arrangement densities: 15 blocks in each row along the y-axis direction, with a total block number of 225, and 16 blocks in each row, with a total block number of 240. The model blocks depicted in Figure 2 were stacked with the former arrangement density. In each row along the onshore x-axis direction, six, five, and four blocks were arranged in the bottom, middle, and top layers, respectively, regardless of the arrangement density.

The incident waves were generated using a flap-type paddle, located at x = 0.0 m as shown in Figure 1. The paddle was driven by a computer-controlled DC servo motor. The reflection coefficient K_r obtained using the Healy method in front of the wave generating paddle is depicted in Figure 4, which indicates that the value of K_r was at most 0.17.

As sketched in Figure 1, four capacitance-type wave gages, namely WGs 1–4, were installed to measure the water surface displacements, which were sampled and recorded every 0.05 s. The wave height measured by WGs 1, 3, and 4 are called the incident wave height, the wave height in front of the breakwater, namely H_f, and the wave

height behind the breakwater, namely H_b, respectively. Two video cameras shot the breakwaters diagonally from both the front and back, recording block shaking, breakwater movement, and how the blocks fell. After stopping the generation of incident waves, the blocks were photographed to record the locations of them. For each case, the experiments were carried out several times and the representative results are presented in this paper.

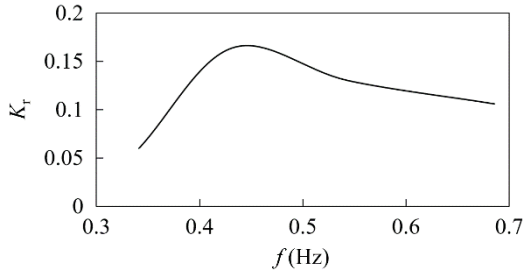

Figure 4. The reflection coefficient K_r in front of the wave generating paddle depicted in Figure 1. The horizontal axis is the frequency of the generated regular waves, f.

2.2 Experimental conditions with incident irregular waves

Irregular waves were incident in Cases eI_{15} and eI_{16}, in which 15 and 16 blocks were arranged in each row along the y-axis direction, respectively. The still water level was 0.925 m, 0.9 m, and 0.87 m, namely the HHWL, HWL, and MWL, respectively, as depicted in Figure 5.

The significant wave height measured by WG 1, H_I, was 0.077 m, 0.094 m, 0.118 m, 0.158 m, 0.167 m, 0.208 m, and 0.258 m, for each still water level. The wave gage distances λ_1 and λ_2 indicated in Figure 1 were 4.0 m and 1.0 m, respectively. The experimental conditions are summarized in Table 2.

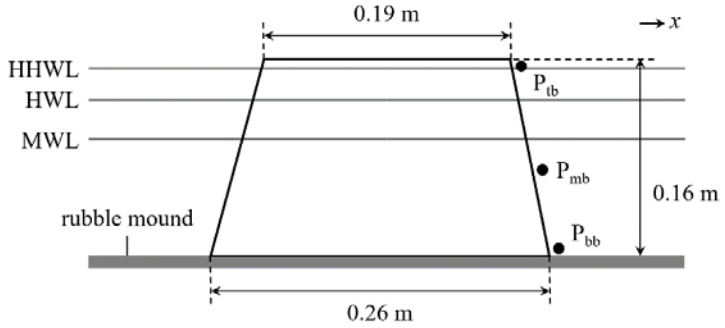

Figure 5. A sketch for the vicinity of the low-top detached breakwater, where the crown height H_c, crown width, and bottom width of the breakwater are 0.16 m, 0.19 m, and 0.26 m, respectively. The still water levels HHWL, HWL, and MWL are located at z = 0.925 m, 0.9 m, and 0.87 m, respectively, where z is 0.0 m at the most offshore horizontal floorboard depicted in Figure 1.

Table 2. The experimental conditions, in which H_I is the significant wave height of the incident irregular waves measured by WG 1 depicted in Figure 1; H_L is the wave height of the incident long waves; T_L is the approximate wave period of the incident long waves. The corresponding values on the field scale are described in the parentheses. The still water levels HHWL, HWL, and MWL were 0.925 m, 0.9 m, and 0.87 m, respectively, N is the number of the blocks in each row along the y-axis direction, and λ_1 and λ_2 are the distances between WGs 2 and 3 and WGs 3 and 4, respectively.

Case	Still Water Level	1st Series of Irregular Waves	Long Wave		2nd Series of Irregular Waves	N	Distances Between Wave Gages	
		H_I (m)	H_L (m)	T_L (s)	H_I (m)		λ_1 (m)	λ_2 (m)
eI_{15}	HHWL HWL MWL	0.077 m–0.258 m (3.31 m–11.09 m)	None	None	None	15	4.0	1.0
eI_{16}						16		
eL	HWL	None	0.045 m–0.193 m (1.94 m–8.30 m)	5.0 s–11.0 s (32.8 s–72.1 s)			4.1	0.7
eIL eLI		0.082 m, 0.132 m (3.53 m, 5.68 m)	0.113 m–0.193 m (4.86 m–8.30 m)	10.0 s (65.6 s)				
eILI					0.082 m, 0.132 m (3.53 m, 5.68 m)			

In both Cases eI_{15} and eI_{16}, irregular waves were generated for 5 min. The spectrum type of the incident irregular waves was the Bretschneider-Mitsuyasu type, represented by

$$E(f) = 0.257 H_{1/3}{}^2 T_{1/3} (T_{1/3} f)^{-5} \exp[-1.03 (T_{1/3} f)^{-4}] \ (\mathrm{m}^2/\mathrm{s}), \quad (1)$$

where E, f, $H_{1/3}$, and $T_{1/3}$ are energy spectrum, wave frequency, significant wave height, and significant wave period, respectively. To drive the wave generating paddle, the signals were obtained using an irregular noise generator with 12 bandpass filters and DA-converted to be input to the servo motor.

2.3 Experimental conditions with an incident long wave

In Case eL, a long wave was generated with no irregular wave. The still water level was the HWL, namely 0.9 m, and 16 wave dissipating blocks were stacked in each row along the *y*-axis direction. The experimental conditions with an incident long wave are also summarized in Table 2.

2.4 Experimental conditions with both incident irregular waves and an incident long wave

In Cases eIL, eLI, and eILI, a long wave was generated in succession with irregular waves. The still water level was the HWL, namely 0.9 m, and 16 wave dissipating blocks were stacked in each row along the *y*-axis direction. In Case eIL, irregular waves were followed by a long wave, whereas in Case eLI, a long wave was followed by irregular waves. In Case eILI, irregular waves were followed by a long wave, and then irregular waves were continuously incident again. The experimental conditions for these cases are also summarized in Table 2.

3. Numerical method and conditions

We performed vertically two-dimensional numerical calculations. Figure 6 illustrates the calculation domain with a length of 46.3 m and a height of 1.5 m, where the scale of length is 1/43. The seabed profile is the same as that in the hydraulic experiments depicted in Figure 1. A low-top detached breakwater was installed on a rubble foundation, where the crown height H_c, crown width, and bottom width of the breakwater were 0.16 m, 0.19 m, and 0.26 m, respectively.

In the numerical calculations, a long wave was generated in Case nL, whereas regular short waves were incident in Case nS, to examine the pressure and velocity fields around the breakwater for different incident wave periods. In Case nL, the incident wave height H_L was 0.1 m, the incident wave period T_L was of 8.0 s, 10.0 s, 12.0 s, and 14.0 s, and the still water level was the HWL, namely 0.9 m. Conversely, in Case nS, the incident wave height H_S was 0.056 m, the incident wave period T_S was 1.7 s, and the still water levels were the HHWL, HWL, and MWL, namely 0.925 m, 0.9 m, and 0.87 m, respectively. The conditions for the numerical calculations are summarized in Table 3.

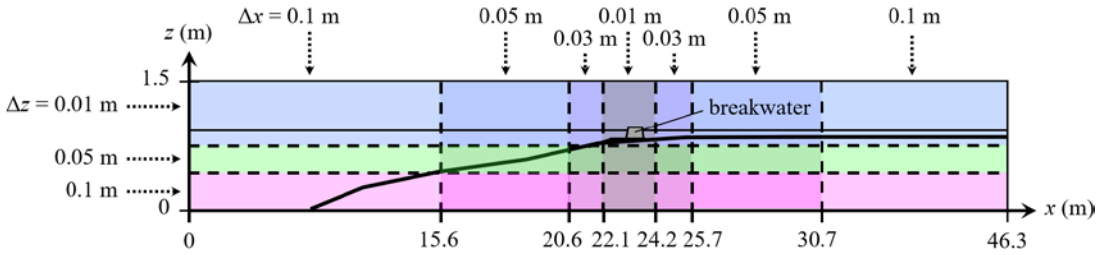

Figure 6. The calculation domain, in which the grid sizes Δx and Δz are described for each column and layer, respectively. The incident waves were generated at x = 0.0 m.

Table 3. The conditions of the numerical calculations, in which H_L and T_L are the wave height and period of the incident long waves, respectively, and H_S and T_S are the wave height and period of the incident regular short waves, respectively. The corresponding values on the field scale are described in the parentheses. The still water levels HHWL, HWL, and MWL were 0.925 m, 0.9 m, and 0.87 m, respectively.

Case	Still Water Level	Long Wave		Regular Short Waves	
		H_L (m)	T_L (s)	H_S (m)	T_S (s)
nL	HWL	0.1 m (4.3 m)	8.0 s, 10.0 s, 12.0 s, 14.0 s (52.5 s, 65.6 s, 78.7 s, 91.8 s)	None	None
nS	HHWL HWL MWL	None	None	0.056 m (2.41 m)	1.7 s (11.1 s)

In the computation, CADMAS-SURF/3D [44, 45] was applied to consider fully nonlinear phenomena, where the Navier-Stokes equations for incompressible fluid motion, as well as the Poisson equation for pressure, were solved numerically in the vertical two dimensions. The volume of fluid (VOF) method was used to express the water surface level. The finite difference equations were solved with a first-order upwind difference scheme.

The calculation domain depicted in Figure 6 was horizontally divided into 7 zones, in which the grid intervals Δx were 0.1 m, 0.05 m, 0.03 m, 0.01 m, 0.03 m, 0.05 m, and 0.1 m from offshore to onshore, respectively. Conversely, the calculation domain was vertically divided into 3 zones, in which the grid intervals Δz were 0.1 m, 0.05 m, and 0.01 m from bottom to top, respectively. The simplified marker and cell (SMAC) method was used for time integration, where the time step interval was automatically determined to satisfy the CFL condition.

The waves were incident using the flap-type wave generating function. The Sommerfeld radiation condition was applied to the lateral boundaries in the x-axis direction. A high Reynolds number type k-ε two-equation model was adopted for turbulence.

The block mound detached breakwater was represented as a porous structure using porous cells. The porosity was 0.5, which was obtained from the block volume, block number, and breakwater volume in the hydraulic experiments described above. The values of the drag coefficient C_D and inertial force coefficient C_M were determined to be 1.0 and 1.2, respectively, by comparing the numerical results with the corresponding experimental data for the water surface displacements behind the breakwater. Figure 7 presents a comparison example of the numerical and experimental water surface displacements for the incident regular waves with a wave period of 2.0 s. The calculated water level for the crests was highly reproducible, although the water level of the troughs was slightly underestimated.

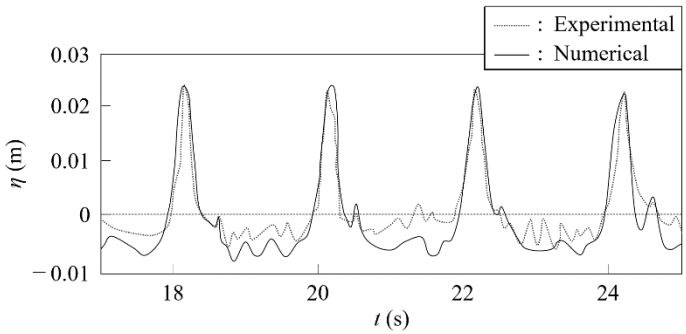

Figure 7. The experimental and numerical water surface displacements behind the breakwater, for the incident regular waves with a wave period of 2.0 s.

4. Response of wave dissipating blocks composing a detached breakwater based on the hydraulic experiments

4.1 Response of wave dissipating blocks composing a detached breakwater to incident irregular waves

4.1.1 Wave height transmission coefficient

We conducted the hydraulic experiments in which the irregular waves were incident when the still water level is of the HHWL, HWL, and MWL. The experimental conditions are listed in Table 2. The significant wave heights of the incident irregular waves measured by WG 1 shown in Figure 1 were 0.077 m, 0.094 m, 0.118 m, 0.158 m, 0.167 m, 0.208 m, and 0.258 m.

Figure 8 depicts the wave height transmission coefficient K_t in Case eI_{16}, in which 16 blocks were arranged in each row along the y-axis direction, where K_t is defined as the ratio of the wave height behind the breakwater, H_b, to that in front of the breakwater, H_f, measured by WGs 4 and 3, respectively, i.e.,

$$K_t = H_b / H_f, \tag{2}$$

where the wave heights are the significant wave heights. In Figure 8, the horizontal axis is the ratio of the breakwater crown height H_c to H_f. For the present wave dissipating blocks, the figure indicates that as the still water level or incident significant wave height was increased, the wave height transmission coefficient K_t showed an increasing trend with a few exceptions.

When the still water level is the HWL, the wave height transmission coefficients K_t in both Cases eI_{15} and eI_{16} are depicted in Figure 9. As indicated in the figure, K_t tended to increase, when the block arrangement density is

decreased. The reason is that when 15 blocks are arranged in each row along the *y*-axis direction, several blocks started to slip down earlier, so K_t increased owing to the flow passing through the collapsed parts of the breakwater.

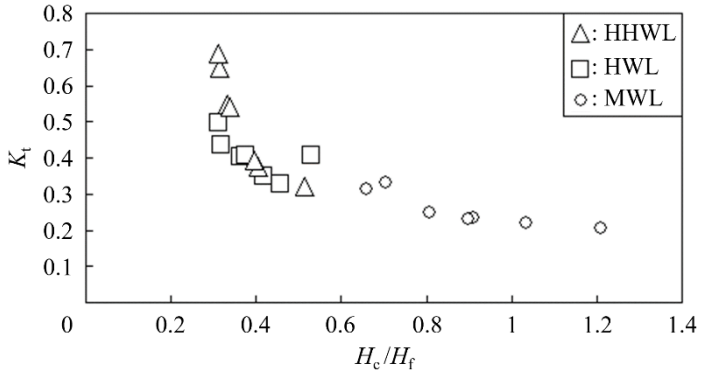

Figure 8. The wave height transmission coefficients K_t for different still water levels and incident significant wave heights in Case eI_{16}, in which the still water levels were the HHWL, HWL, and MWL, namely 0.925 m, 0.9 m, and 0.87 m, respectively. The horizontal axis is the ratio of the breakwater crown height H_c to the significant wave height in front of the breakwater, H_f, measured by WG 3 shown in Figure 1, in which λ_1 was 4.0 m. The significant wave heights of the incident irregular waves were 0.077 m, 0.094 m, 0.118 m, 0.158 m, 0.167 m, 0.208 m, and 0.258 m. In each row along the *y*-axis direction, 16 blocks were arranged to build the breakwater.

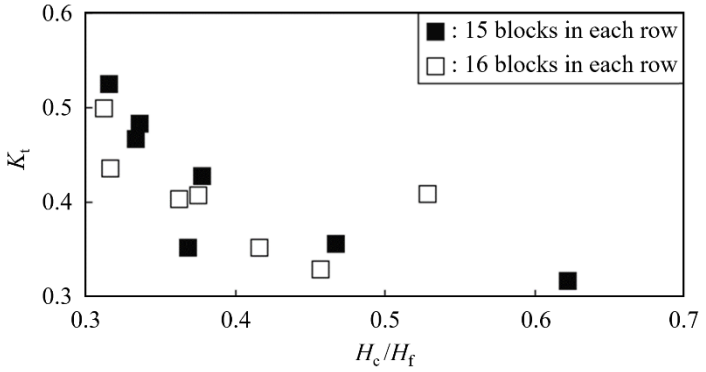

Figure 9. The wave height transmission coefficients K_t for different block arrangement densities when the still water level is the HWL, namely 0.9 m, in Cases eI_{15} and eI_{16}, in which 15 and 16 blocks were arranged in each row along the *y*-axis direction, respectively. The horizontal axis is the ratio of the breakwater crown height H_c to the significant wave height in front of the breakwater, H_f, measured by WG 3 shown in Figure 1, in which λ_1 was 4.0 m. The significant wave heights of the incident irregular waves were 0.077 m, 0.094 m, 0.118 m, 0.158 m, 0.167 m, 0.208 m, and 0.258 m.

Moreover, the influence of the armor unit placement on the armour stability was investigated [46], so, great care was taken when loading the blocks. Based on the video footage, several data deviating from the trends in Figures 8 and 9 were due to abrupt large waves. When there were subtle differences in how the blocks were stacked, such as the installation angle, the number of deviating data was much larger. Therefore, it was reconfirmed that stacking blocks in the field requires both sufficient block arrangement density and great care to the meshing of the blocks, to enhance the wave protection function of block mound breakwaters.

4.1.2 Fallen block locations

The fallen block locations after stopping the generation of the irregular waves with a significant wave height of 0.258 m in both Cases eI_{15} and eI_{16} are depicted in Figure 10, in which δ is the distance in the *x*-axis direction from the shore end of the breakwaters. First, when the still water level is the lowest, namely the MWL, a large overflow was unlikely to occur, so all the blocks remained in mesh without falling in Case eI_{16}, in which 16 blocks were arranged in each row along the *y*-axis direction. Conversely, in Case eI_{15} with a lower block arrangement density, 9 blocks fell near the breakwater side ends, although the central part of the breakwater was stable with no block falling. The reason was that the blocks at both ends of the breakwater were not engaged with the flume side walls, and the end blocks that were not sufficiently held by the adjacent blocks slid down.

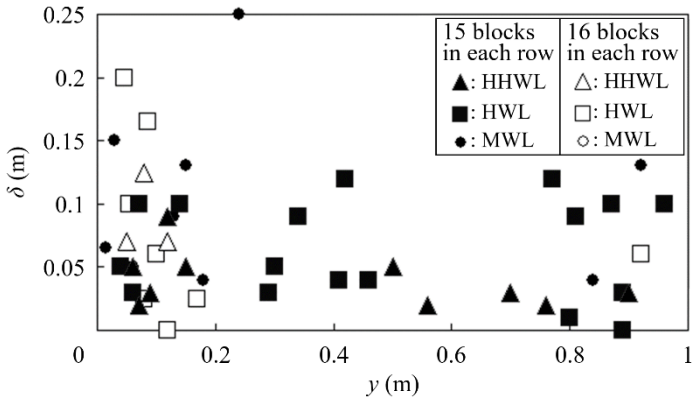

Figure 10. The fallen block locations for the incident irregular waves with a significant wave height of 0.258 m in Cases eI_{15} and eI_{16}, in which 15 and 16 blocks were arranged in each row along the *y*-axis direction, respectively. The vertical axis δ is the distance in the *x*-axis direction from the shore end of the breakwaters. The still water levels were the HHWL, HWL, and MWL, namely 0.925 m, 0.9 m, and 0.87 m, respectively.

Second, as indicated in Figure 10, when the still water level is in the middle, namely the HWL, the number of the fallen blocks was larger than those in the cases with the other still water levels for both block arrangement densities. When the still water level is the HWL, the wave breaking often occurred just in front of the breakwater, not offshore as in the cases with the MWL, so the wave energy of many waves did not decay much in the breaker zones before the waves hit the breakwaters. Moreover, in the cases with the HWL, the overflow was the most effective to slip down the blocks owing to not only the smaller decay in wave energy but also the adequate water depth over the breakwater, not too deep as in the cases with the HHWL. This is why many blocks, including the blocks stacked in the breakwater center, fell with the HWL. In the present experiments with the blocks depicted in Figure 3, the transmitted wave height approximately increased as the water depth was increased in *Section 4.1.1*, as assumed in [3] when deriving the empirical formula for transmitted wave height. However, the block response is not necessarily linearly related to water depth, so block mound breakwaters should be designed considering both the block characteristics and possible water depths where the breakwaters will be installed.

Third, when the still water level is the largest, namely the HHWL, the low-top detached breakwater was completely submerged during the overflow. Because this led to the weaker effect of the flow over the breakwater, the blocks did not fall easily.

To summarize the effects of the still water level, the block falling is most likely to occur at moderately high still water levels, such as the HWL. Therefore, even when the water level does not rise as high as an HHWL, it is necessary to keep in mind that block mound detached breakwaters can be damaged, leading to the invasion of large waves.

4.2 Response of wave dissipating blocks composing a detached breakwater to an incident long wave

4.2.1 Water surface profiles of the incident long waves

A long wave was incident in Case eL, the conditions of which are described in Table 3. Figure 11 depicts four examples of the offshore water surface displacements measured by WG 1 shown in Figure 1, where the incident wave period was approximately 5.0 s. The distance to move the wave generating paddle, which determined the incident wave height for each wave period, was changed by the total amplitude of the wave generating signal voltage, *V*. The incident wave heights of the long waves depicted in Figure 11 are 0.113 m, 0.138 m, 0.165 m, and 0.193 m, using the zero-upcrossing method.

Figure 12 presents the water surface displacements measured by WG 3 in front of the breakwater shown in Figure 1, for the incident long waves depicted in Figure 11. The incident long waves propagated over the slopes with shallowing, and then wave breaking occurred offshore from the breakwater, so the waves depicted in Figure 12 are broken waves with a bore.

4.2.2 Wave height transmission coefficient

The wave height transmission coefficients K_t defined by Eq. (2), for different incident long wave heights H_L and periods T_L in Case eL, were depicted in Figure 13, in which the horizontal axis is the ratio of the breakwater crown height H_c to the wave height in front of the breakwater, H_f, measured by WG 3 depicted in Figure 1. The still water level was the HWL, and 16 blocks were arranged in each row along the *y*-axis direction. This figure

indicates the tendency that K_t for each incident wave period T_L increased, as the incident wave height H_L was increased. In the long wave cases, the irregularities might also be due to the unstable broken waves with a bore.

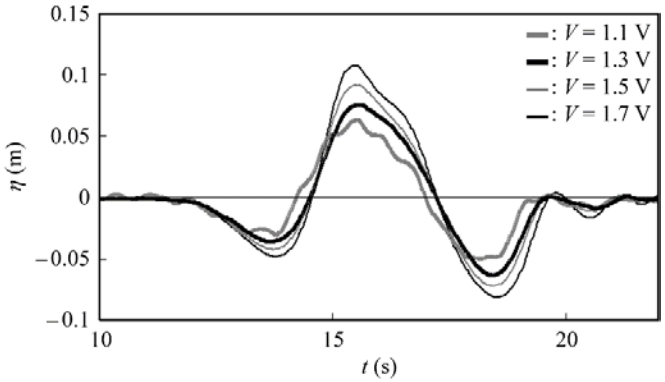

Figure 11. Examples of the offshore water surface displacements measured by WG 1 depicted in Figure 1, for different total amplitudes of the wave generating signal voltage, *V*. The period of the incident long waves was approximately 5.0 s, and the still water level was the HWL, namely 0.9 m.

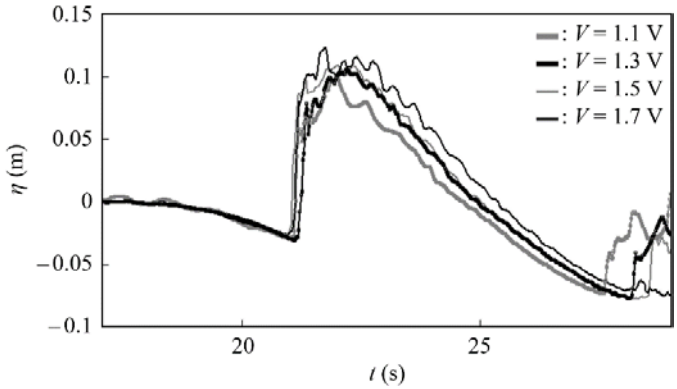

Figure 12. The water surface displacements measured by WG 3 in front of the breakwater depicted in Figure 1, for the incident long waves depicted in Figure 11. The wave gage distance λ_1 indicated in Figure 1 was 4.1 m.

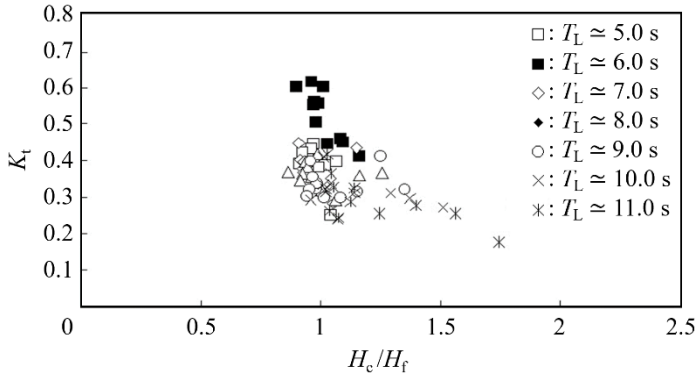

Figure 13. The wave height transmission coefficients K_t for different incident long wave heights H_L and periods T_L in Case eL, in which H_L was 0.045 m to 0.193 m and T_L was approximately 5.0 s to 11.0 s. The still water level was the HWL, namely 0.9 m, and 16 blocks were arranged in each row along the *y*-axis direction. The horizontal axis is the ratio of the breakwater crown height H_c to the wave height in front of the breakwater, H_f, measured by WG 3 depicted in Figure 1, in which λ_1 was 4.1 m.

4.2.3 Total number of the fallen blocks

Figure 14 depicts the total numbers *n* of the fallen blocks for different incident long wave heights H_L and periods T_L in Case eL, where T_L was approximately 5.0 s to 10.0 s. The still water level was the HWL, and 16 blocks were arranged in each row along the *y*-axis direction. When the incident wave period T_L is approximately 11.0 s, no block fell, which is not shown in the figure. As the incident wave height H_L was increased, the total number *n* for

each incident wave period T_L tended to increase, owing to the larger energy of the overtopping long waves. It should be noted that n did not increase unconditionally as the incident wave period T_L was increased: for example, in the cases where H_c/H_L = 1.28, n was the largest when T_L is approximately 7.0 s, and when T_L is approximately 8.0 s, 6.0 s, and 5.0 s, n decreased in this order.

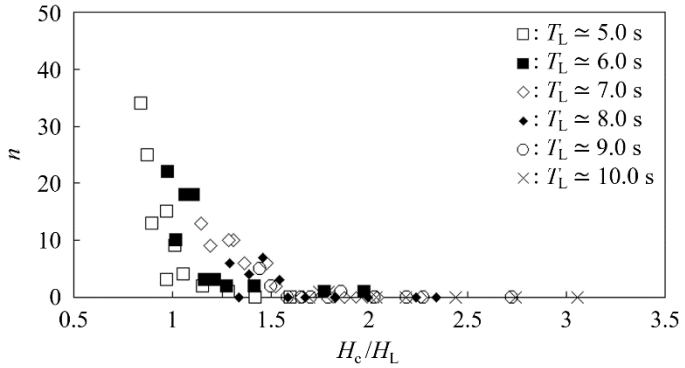

Figure 14. Total numbers of the fallen blocks, n, for different incident long wave heights H_L and periods T_L in Case eL, where H_L was 0.045 m to 0.193 m, and T_L was approximately 5.0 s to 10.0 s. The still water level was the HWL, namely 0.9 m, and 16 blocks were arranged in each row along the y-axis direction. The horizontal axis is the ratio of the breakwater crown height H_c to H_L.

First, when the incident wave period T_L is approximately 10.0 s and 11.0 s, and the incident wave height H_L is smaller than 0.06 m, no wave overtopped the breakwater, so the wave height transmission coefficient K_t was small as indicated in Figure 13. Moreover, Figure 14 indicates that almost no block slipped down when T_L is approximately 10.0 s and H_L is smaller than 0.06 m. Therefore, when T_L is approximately 10.0 s and 11.0 s in the present cases, water passed through the gaps between the almost fixed blocks while the long waves passed by the breakwater.

Second, when the incident wave height H_L is 0.06 m to 0.08 m, unbroken waves propagated to the breakwater, and then the overtopping waves shook the blocks placed on the shore side, namely at the back of the breakwater.

Third, when the incident wave height H_L is larger than 0.08 m, the long waves showed wave breaking offshore from the breakwater. Thereafter, the broken waves violently hit the breakwater, with a water flow crawling in front of the breakwater, and a flow over the breakwater was generated. The overflow lasted for a long time while the pushing waves passed by the breakwater, and the entire breakwater was slightly lifted and shifted toward the shore, resulting in weaken block meshing. Thus, many of the blocks placed at the back of the breakwater slipped down. Moreover, during the offshore flow due to the pulling wave after the pushing wave, the water level rose and fell behind and before the breakwater, respectively, lowering the water level in the breakwater toward offshore. The water surface gradient in the breakwater increased as the incident wave period T_L was decreased. Both the offshore flow of the pulling wave and the water surface gradient in the breakwater carried several gravels placed below the breakwater toward offshore.

4.3 Response of wave dissipating blocks composing a detached breakwater when irregular waves and a long wave are continuously incident

4.3.1 Block sliding when irregular waves and a long wave are continuously incident in this order

Irregular waves and a long wave were continuously incident in this order in Case eIL, the conditions of which are described in Table 2. When the significant wave height of the incident irregular waves, H_I, is as small as 0.082 m, although the blocks were hardly moved by the irregular waves, several blocks were slid by the subsequent long wave. Conversely, when H_I is as large as 0.132 m, several blocks were fallen by the irregular waves, and then many blocks placed at the back of the breakwater were dropped by the following long wave, expanding the damaged part of the breakwater.

4.3.2 Block sliding when irregular waves, a long wave, and irregular waves are continuously incident in this order

The first series of irregular waves, a long wave, and the second series of irregular waves were continuously incident in this order in Case eILI, the conditions of which are described in Table 2. Figure 15 presents an example of the water surface displacement measured by WG 3 in front of the breakwater depicted in Figure 1. The significant wave height of the incident irregular waves, H_I, was 0.082 m, whereas the wave height H_L and period T_L of the incident long wave were 0.193 m and approximately 10.0 s, respectively.

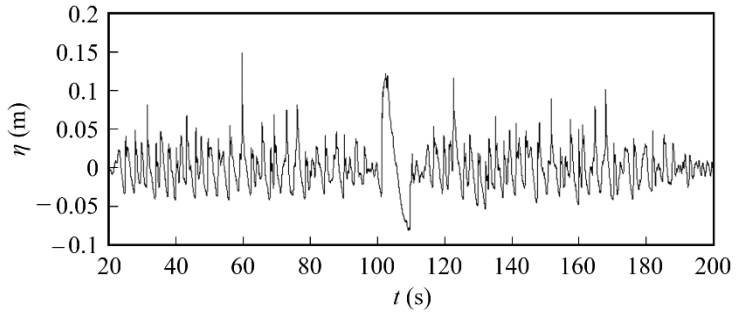

Figure 15. An example of the water surface displacement η, measured by WG 3 in front of the breakwater depicted in Figure 1, in Case eILI, in which λ_1 was 4.1 m. The significant wave height of the incident irregular waves, H_I, was 0.082 m, whereas the wave height H_L and period T_L of the incident long wave were 0.193 m and approximately 10.0 s, respectively. The still water level was the HWL, namely 0.9 m.

The total numbers of the fallen blocks, n, in Case eILI are depicted in Figure 16, in which the horizontal axis is the ratio of the significant wave height of the incident irregular waves, H_I, to the wave height of the incident long wave, H_L. As described in *4.2.3*, when the incident long wave height H_L is larger than 0.08 m, the long waves showed wave breaking offshore from the breakwater, so long broken waves propagated to the breakwater in Case eILI. Based on Figure 16, the total number of the fallen blocks, n, was 10 or 11 when H_I is 0.132 m and H_L is 0.193 m, whereas n was 5 or 6 when H_I is 0.082 m and H_L is 0.193 m. Conversely, based on Figure 10 in Case eI_{16}, n was 8 when the irregular waves with significant wave height H_I of 0.258 m are incident with the HWL for 5 min. Therefore, comparing these results, the long wave following the irregular waves is effective, because 10 or 11 blocks cannot be dropped by the long wave alone or the irregular waves alone.

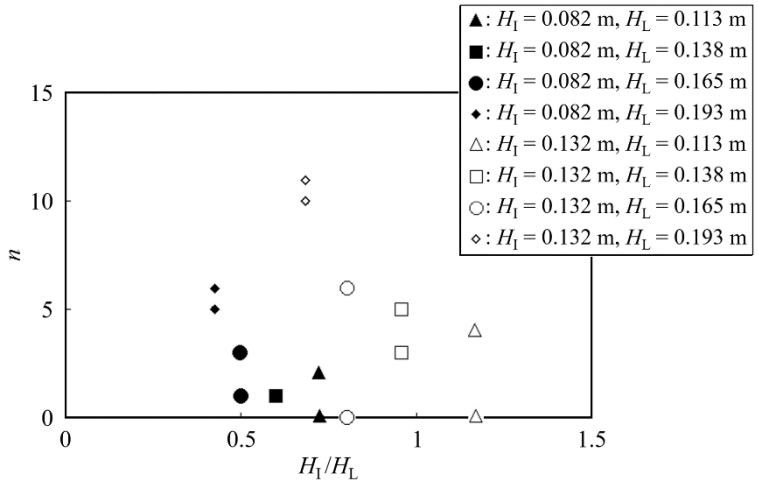

Figure 16. The total numbers of the fallen blocks, n, in Case eILI, in which the incident long wave period T_L was approximately 10.0 s. The significant wave height of both the first and second series of the incident irregular waves, H_I, was of 0.082 m and 0.132 m, whereas the incident long wave height H_L was 0.113 m to 0.193 m. The still water level was the HWL, namely 0.9 m, and 16 blocks were arranged in each row along the y-axis direction.

When the significant wave height of the incident irregular waves, H_I, is as large as 0.132 m, the first irregular wave train shifted several blocks, and the following long wave dropped these shifted blocks, displacing the blocks around them. Then, the second irregular wave train dropped many of the displaced blocks. Under several conditions, the total number of the fallen blocks, n, in Case eILI was more than five times as much as that with the corresponding conditions in Case eLI, in which a long wave and irregular waves were continuously incident in this order. This suggests that when the displacements of blocks accumulate because of large waves due to one or several severe storms, the blocks may easily be slid down by harbor oscillations and swells caused by a subsequent storm. Therefore, sufficient caution is required to the conditions of block mound breakwaters when a series of violent storms generate not only large short waves but also long waves like swells.

5. Wave pressure and velocity vectors around a detached permeable breakwater based on the numerical calculations

5.1 Wave pressure and velocity vectors around a detached permeable breakwater when a long wave is incident

We generated vertically two-dimensional numerical simulations to obtain both the wave pressure and velocity vectors around a permeable detached breakwater in Cases nL and nS, the conditions of which were determined based on the experimental results and are listed in Table 3.

First, regarding Case nL, the still water level was the HWL, namely 0.9 m, and a long wave with various wave periods was incident. In the hydraulic experiments with the incident long waves, the blocks near the top of the back of the breakwater usually slid first, so we especially focus on the numerical results of the wave pressure at the top behind the breakwater, p_{tb}, at Point P_{tb} indicated in Figure 5. In the present paper, "wave pressure" is defined as total pressure minus pressure under still water conditions, so the wave pressure can be positive, zero, and negative.

Figure 17 depicts the numerical results for the time variations of p_{tb}, for different incident long wave periods T_L. As indicated in the figure, the negative wave pressure appeared at the top behind the breakwater. When the incident wave period T_L is 8.0 s, 10.0 s, and 12.0 s, the maximum absolute value of the negative wave pressure generated at the top behind the breakwater, $|p_{tb}|_{max}$, increased, as T_L was increased.

The incident wave started wave breaking at $t = t_B$, whereafter the broken wave collided with the breakwater at $t = t_C$. The wave breaking time t_B and collision time t_C are described in Table 4, for each incident wave period T_L. This table also describes the distance d_B between the wave breaking point and the offshore end of the breakwater. As the incident wave period T_L was increased, both the wave breaking time t_B and collision time t_C were later, and the wave breaking point approached the breakwater. In any condition of Case nL, the waves showed a plunging type of wave breaking offshore from the breakwater, and a bore was generated and existed near the water surface in the breaker zone. Therefore, assuming that there was not much difference in the energy reduction during the wave breaking in these cases, as T_L was increased, the ratio of energy decay to total energy of the broken waves before hitting the breakwater decreased owing to the shorter distance d_B. As a result, a larger overflow generated larger $|p_{tb}|_{max}$ as T_L was increased when T_L is 8.0 s, 10.0 s, and 12.0 s. However, $|p_{tb}|_{max}$ when T_L is 14.0 s was smaller than that when T_L is 12.0 s, the reason of which will be discussed later.

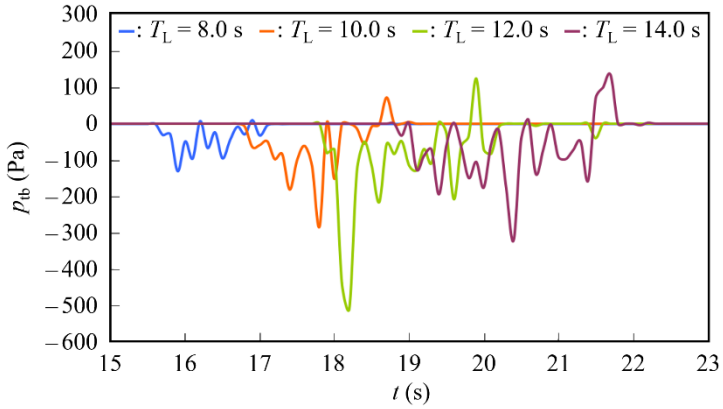

Figure 17. Numerical results for the time variations of the wave pressure at the top behind the breakwater, p_{tb}, for different incident long wave periods T_L in Case nL. The still water level was the HWL, namely 0.9 m, and the incident wave height H_L was 0.1 m.

Table 4. The wave breaking time t_B, the collision time t_C, and the distance between the wave breaking point and the offshore end of the breakwater, d_B, for each incident wave period T_L in Case nL.

T_L	t_B	t_C	d_B
8.0 s	11.4 s	15.4 s	4.5 m
10.0 s	13.1 s	16.5 s	4.1 m
12.0 s	14.1 s	17.5 s	4.0 m
14.0 s	15.0 s	18.7 s	3.8 m

Depicted in Figure 18 are the time variations of the wave pressures p at the top, middle, and bottom behind the breakwater, namely p_{tb}, p_{mb}, and p_{bb} at Points P_{tb}, P_{mb}, and P_{bb} indicated in Figure 5, respectively, for each incident wave period T_L. As indicated in the figures, negative wave pressure was predominantly generated at the top behind

the breakwater, although the wave pressure fluctuated between positive and negative values at both the middle and bottom behind the breakwater. All the wave pressures p_{tb}, p_{mb}, and p_{bb} showed the minimum values before the maximum values. When T_L is 8.0 s, the negative wave pressures were not so small, and the subsequent positive wave pressures with larger absolute values lasted longer. In such a case, even when several blocks are moved slightly by the negative wave pressures, they can then be returned to their original positions by the positive wave pressures. The positive wave pressure below the top behind the breakwater, including p_{mb} and p_{bb}, will also be effective to repair the breakwater. Conversely, when the minimum value of p_{tb} is sufficiently small, as when T_L is 12.0 s, irreversible falls of blocks can occur. The minimum value of p_{tb} was smaller when T_L is 12.0 s than when T_L is 14.0 s, so more blocks fell in the former case.

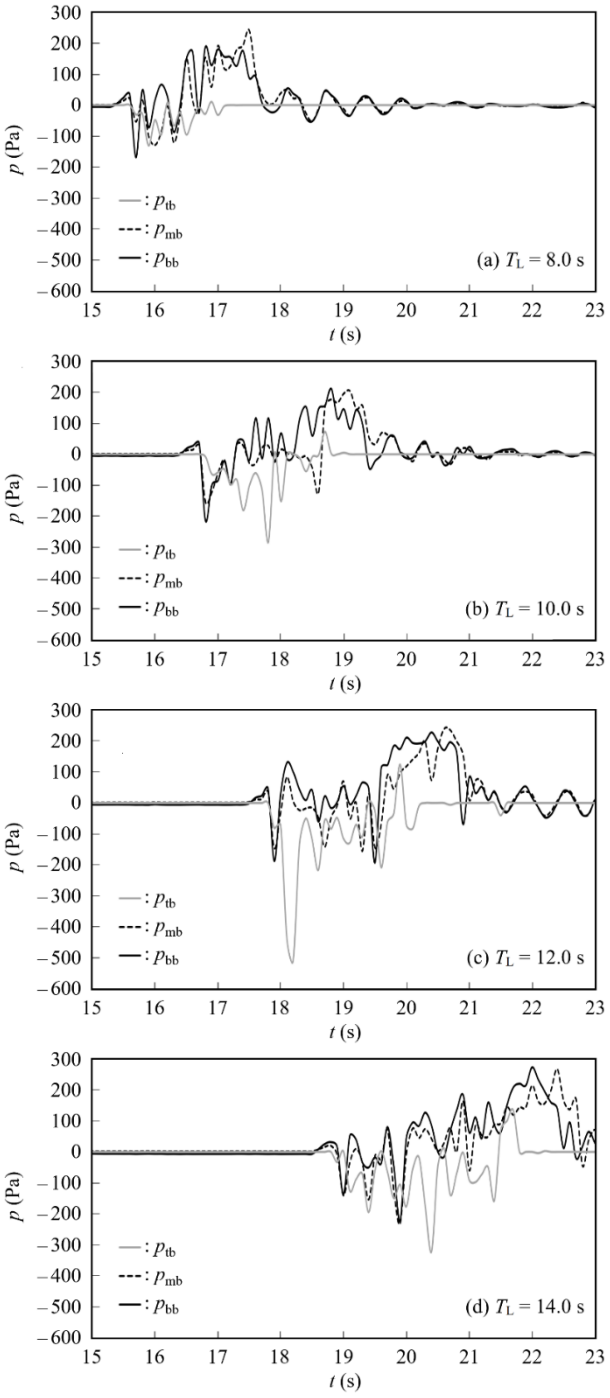

Figure 18. Time variations of the pressures p at the top, middle, and bottom behind the breakwater, namely p_{tb}, p_{mb}, and p_{bb} at Points P_{tb}, P_{mb}, and P_{bb} indicated in Figure 5, respectively, for each incident long wave period T_L in Case nL. The still water level was the HWL, namely 0.9 m, and the incident wave height H_L was 0.1 m.

Figures 19–22 present the distributions of wave pressure p and the vectors of velocity $\boldsymbol{v}$ in the vicinity of the breakwater, when the pressure at the top behind the breakwater, p_{tb}, showed the lowest value, for each incident long wave period T_L in Case nL. The stepped shape of the breakwater drawn in the figures for the velocity vectors was levelled by using porous cells in the numerical calculations. As indicated by the velocity vectors, the velocity increases especially near the top behind the breakwater: for example, in Figure 21(b), the maximum velocity is 1.19 m/s at the top behind the breakwater when T_L is 12.0 s. Such a large velocity generated the negative wave pressure near the top behind the breakwater in all the cases.

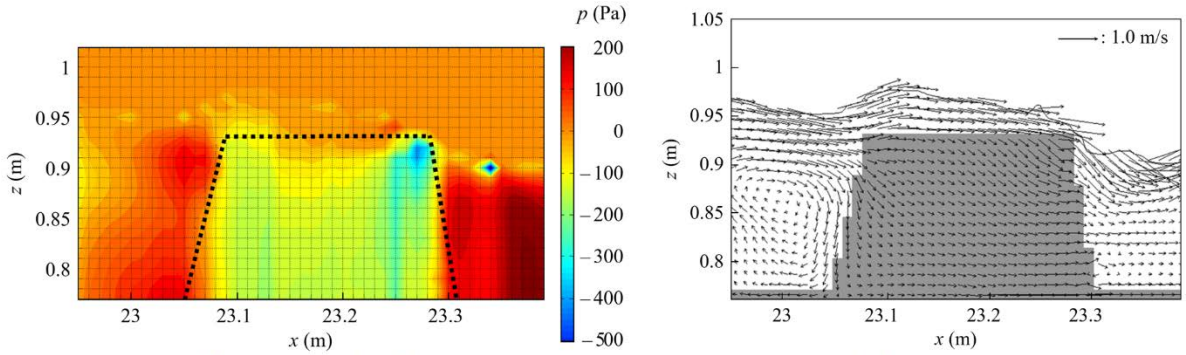

(a) Wave pressure distribution (b) Velocity vectors

Figure 19. The wave pressure distribution and velocity vectors in the vicinity of the breakwater, when the wave pressure at the top behind the breakwater, p_{tb}, showed the lowest value, for the incident long wave with wave period T_L of 8.0 s in Case nL. The still water level was the HWL, namely 0.9 m, and the incident wave height H_L was 0.1 m.

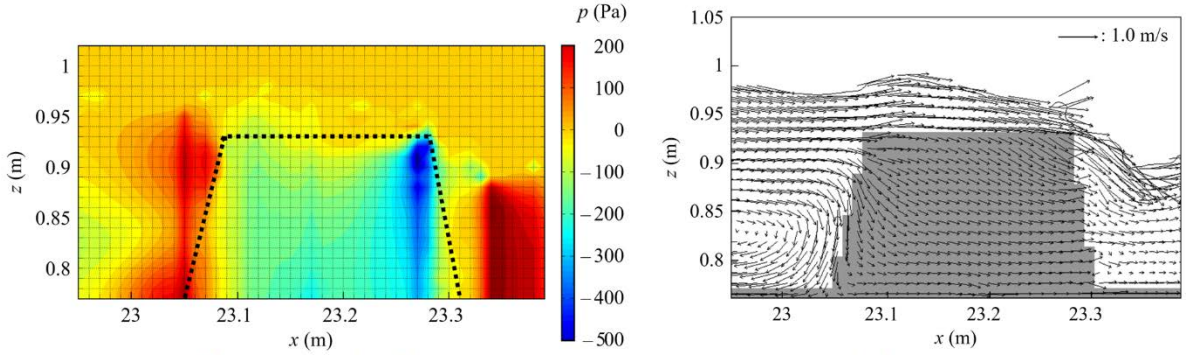

(a) Wave pressure distribution (b) Velocity vectors

Figure 20. The wave pressure distribution and velocity vectors in the vicinity of the breakwater, when the wave pressure at the top behind the breakwater, p_{tb}, showed the lowest value, for the incident long wave with wave period T_L of 10.0 s in Case nL. The still water level was the HWL, namely 0.9 m, and the incident wave height H_L was 0.1 m.

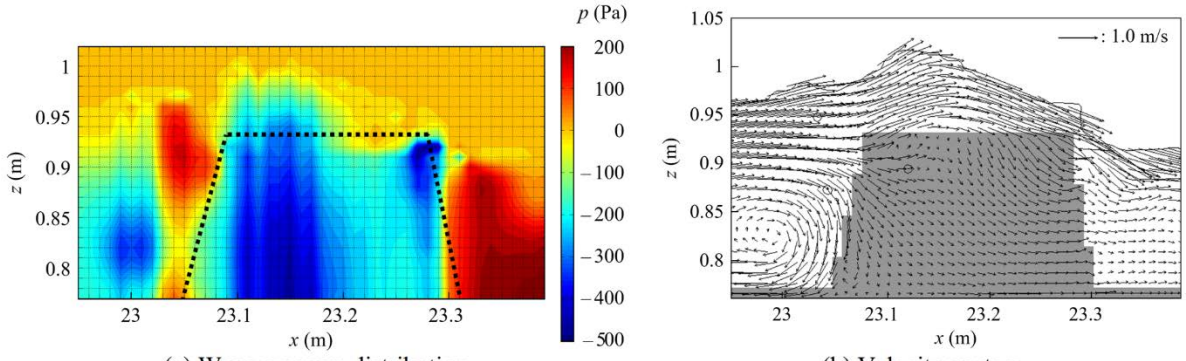

(a) Wave pressure distribution (b) Velocity vectors

Figure 21. The wave pressure distribution and velocity vectors in the vicinity of the breakwater, when the wave pressure at the top behind the breakwater, p_{tb}, showed the lowest value, for the incident long wave with wave period T_L of 12.0 s in Case nL. The still water level was the HWL, namely 0.9 m, and the incident wave height H_L was 0.1 m.

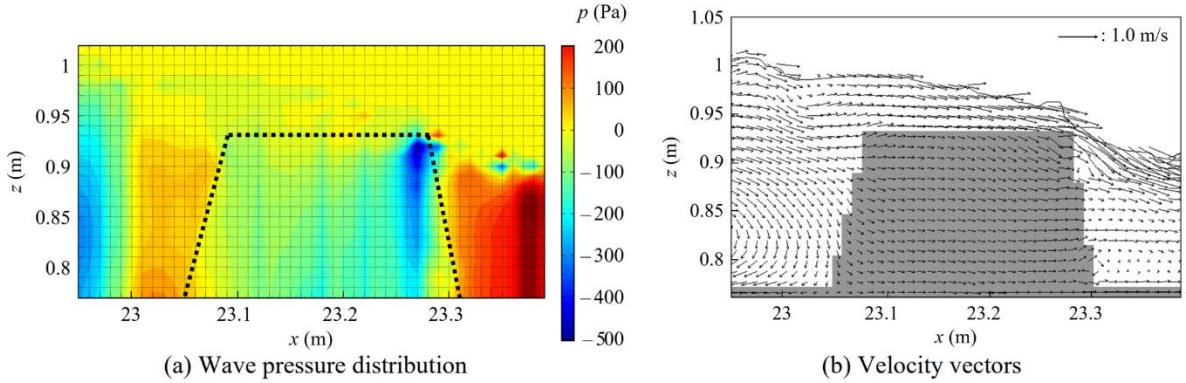

Figure 22. The wave pressure distribution and velocity vectors in the vicinity of the breakwater, when the wave pressure at the top behind the breakwater, p_{tb}, showed the lowest value, for the incident long wave with wave period T_L of 14.0 s in Case nL. The still water level was the HWL, namely 0.9 m, and the incident wave height H_L was 0.1 m.

The figures for the velocity vectors also indicate that a large-scale vortex was created near the seabed in front of the breakwater in every case. The time variation of the velocity field when T_L is 12.0 s is depicted in Figure 23, which reveals that a large-scale vortex appeared when the long waves collided on the breakwater. At t = 17.6 s, the large-scale vortex was clearly generated in front of the breakwater, and then the vortex was stretched offshore. It should be noted that the large-scale vortex remained near the seabed in front of the breakwater during the pushing wave. The vortex remained at t = 18.1 s, at which the vortex center was located at (x, z) ≃ (22.95 m, 0.82 m) and the offshore edge of the vortex was at x ≃ 22.75 m. A water mass was transported upward in front of the remaining large-scale vortex, and moved toward onshore over the large-scale vortex, as if guided by the vortex, resulting in the large onshore flow over the breakwater without large reflection at the breakwater.

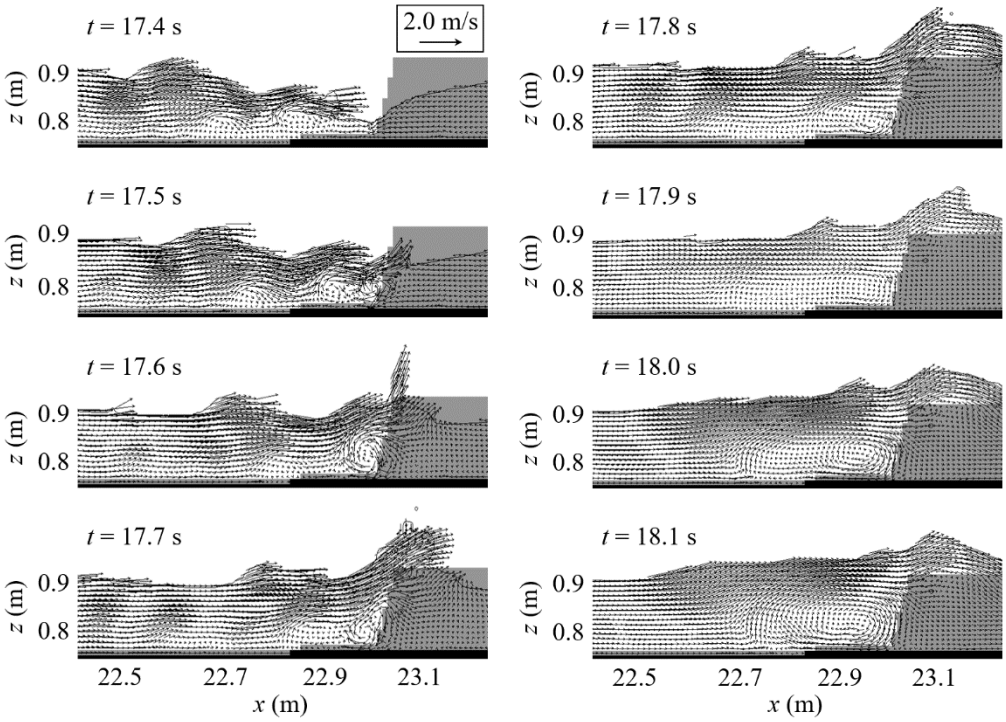

Figure 23. Time variation of the velocity field in front of the breakwater, for the incident long wave with wave period T_L of 12.0 s in Case nL. The still water level was the HWL, namely 0.9 m, and the incident wave height H_L was 0.1 m.

Conversely, in the tsunami simulations [31, 32], although a large-scale vortex appeared in front of a detached breakwater, the vortex disappeared shortly after the tsunami struck the breakwater because of the tsunami's flow almost uniform from the water surface to the seabed, or the milder front slope of the breakwater.

Moreover, the velocity field can be different if the influence of the preceding pulling wave is large. For example, in the tsunami simulation around a submerged breakwater [47], when the onshore flow caused by the subsequent pushing wave crossed the breakwater under the offshore flow due to the preceding pulling wave, a large-scale vortex, rotating in the opposite direction to the vortex described above, was generated below the offshore flow.

In Figures 19(a) and 20(a), the wave pressure is large from top to bottom in front of the breakwater, which means that the waves pushed the large-scale vortex on the breakwater's front face. In Figure 21(a), the wave pressure remarkably increases near the top in front of the breakwater, which indicates that the flow was smoothly guided above the breakwater, resulting in the largest value of $|p_{tb}|_{max}$ when T_L is 12.0 s, as described for Figure 17. In this case, the wave pressure increases both in front of and behind the breakwater, and decreases above the front part of the breakwater. Such a distribution of wave pressure could lift the breakwater in the hydraulic experiments. Conversely, in Figure 22(a), the wave pressure does not increase so much in front of the breakwater, because the center of the large-scale vortex is located far from the breakwater and the velocity in the large-scale vortex is smaller. Therefore, the large-scale vortex was not effective to generate an overflow, resulting in the smaller $|p_{tb}|_{max}$ when T_L is 14.0 s than that when T_L is 12.0 s.

Furthermore, in Figs. 19–22, the overflows show slightly downward velocities near the top behind the breakwater, generating negative wave pressure. Such flows can effectively fall the blocks near the top behind the breakwater without engagement behind. This suggests the need to reinforce the top at the back of the breakwater to make it tenacious, as investigated by e.g. [33] against tsunamis.

Figure 24 depicts the time variations of the horizontal velocity at the top behind the breakwater, u_{tb}, for different incident long wave periods T_L in Case nL. The maximum values of u_{tb} were similar regardless of T_L, although the minimum values of p_{tb} were different depending on T_L as shown in Figure 17.

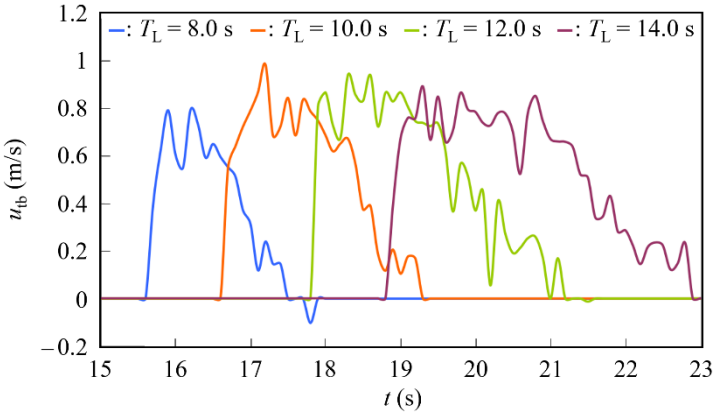

Figure 24. Time variations of the horizontal velocity u_{tb} at Point P_{tb} indicated in Figure 5, for different incident long wave periods T_L in Case nL. The still water level was the HWL, namely 0.9 m, and the incident wave height H_L was 0.1 m.

5.2 Wave pressure and velocity vectors around a detached permeable breakwater when regular short waves are incident

Second, regarding Case nS, we performed numerical calculations to investigate the effect of still water level on the flow fields due to waves around the permeable detached breakwater. We generated regular short waves to examine the fundamental characteristics depending on the still water level. The conditions of Case nS are summarized in Table 3: the still water levels were the HHWL, HWL, and MWL, namely 0.925 m, 0.9 m, and 0.87 m, respectively, whereas the incident wave height H_S and period T_S were 0.056 m and 1.7 s, respectively.

Figure 25 presents the wave pressures at the top, middle, and bottom behind the breakwater, namely p_{tb}, p_{mb}, and p_{bb}, respectively, at Points P_{tb}, P_{mb}, and P_{bb} indicated in Figure 5, respectively, for each still water level in Case nS.

As indicated in Figure 25(c), when the still water level is the lowest, namely the MWL, no overtopping occurred, and the absolute values of both the wave pressures p_{mb} and p_{bb} were smaller than 50.0 Pa. This is consistent with that block falling was not observed at the central part of the breakwater in the hydraulic experiments for the incident irregular waves with the MWL, as described in *4.1.2*. Conversely, as indicated in Figures 25(a) and 25(b), when the still water levels are the HHWL and HWL, the breakwater crown was submerged for a long time, and the wave pressure p_{tb} also showed negative values. Within the time of Figures 25(a) and 25(b), although the minimum value of p_{tb} was smaller with the HHWL than that with the HWL, the minimum values of p_{mb} and p_{bb} were smaller with the HWL than those with the HHWL, respectively. Moreover, the time when p_{mb} and p_{bb} were positive with the

HHWL was longer than those with the HWL, respectively. Therefore, the reasons why the number of the fallen blocks was the largest with the HWL in the hydraulic experiments are as follows:

(a) The local minimums of p_{tb} were often small sufficiently to slide the blocks.

(b) The wave pressure below the top behind the breakwater often caused irreversible block movements.

Based on the video footage of the hydraulic experiments with the HWL, regarding (a), large waves dropped blocks in one shot. Conversely, regarding (b), the column of three blocks at the back of the breakwater often shifted backward.

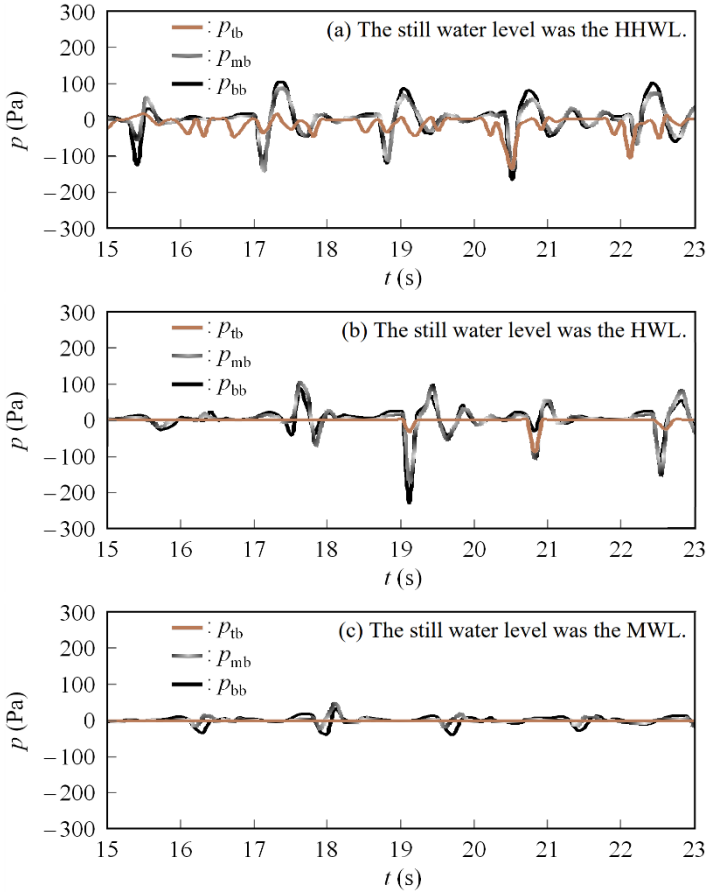

Figure 25. Time variations of the wave pressures at the top, middle, and bottom behind the breakwater, namely p_{tb}, p_{mb}, and p_{bb} at Points P_{tb}, P_{mb}, and P_{bb} indicated in Figure 5, respectively, in Case nS. The still water levels were the HHWL, HWL, and MWL, namely 0.925 m, 0.9 m, and 0.87 m, respectively. The wave height H_S and period T_S of the incident regular short waves were 0.056 m and 1.7 s, respectively.

Figure 26 depicts the wave pressure distribution and velocity vectors in the vicinity of the breakwater when the wave pressure at the top behind the breakwater, p_{tb}, showed a local minimum in Case nS, where the still water level was the HWL, namely 0.9 m. The stepped shape of the breakwater drawn in Figure 26(b) was levelled by using porous cells in the numerical calculation.

Figure 26(a) indicates that the negative wave pressure was generated from top to bottom just behind the breakwater. This distribution was different from those depicted in Figs. 19–22, in which the wave pressure due to the incident long waves was positive at least near the seabed behind the breakwater.

Conversely, Figure 26(b) indicates that the overflow velocity was the largest at the top behind the breakwater, as in the cases with the incident long waves. When the short waves are incident with the HWL, the waves with a large wave height caused overtopping, resulting in the frequent generation of negative wave pressure from top to bottom behind the breakwater, although the duration of each overflow was short. This is consistent with the hydraulic experimental results with the incident large irregular waves, where the blocks at the back of the breakwater were slowly shifted and the block engagement was gradually loosened, leading to the block falling especially at the top of the back of the breakwater.

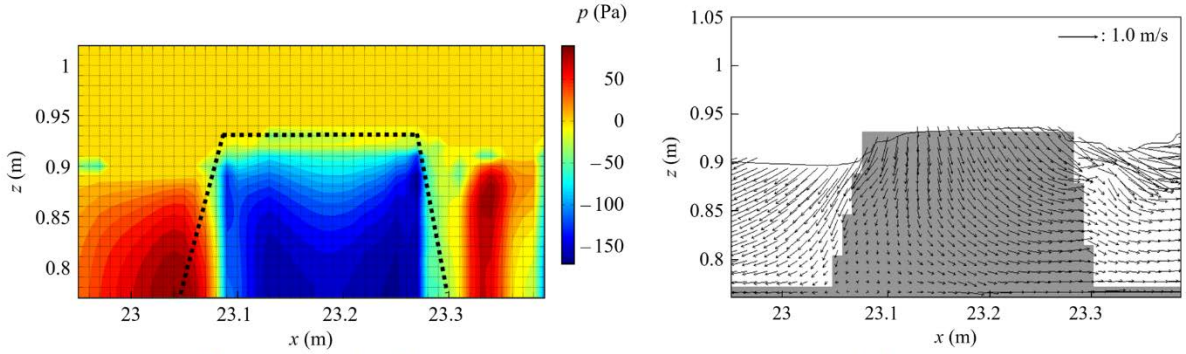

(a) Wave pressure distribution (b) Velocity vectors

Figure 26. The wave pressure distribution and velocity vectors in the vicinity of the breakwater at t = 22.6 s when the wave pressure at the top behind the breakwater, p_{tb}, showed a local minimum in Case nS. The still water level was the HWL, namely 0.9 m, and the wave height H_S and period T_S of the incident regular short waves were 0.056 m and 1.7 s, respectively.

6. Conclusions

The response of the wave dissipating blocks composing a low-top detached breakwater to the incident waves with various periods was investigated based on both the experimental and numerical results.

We first conducted the hydraulic experiments in which irregular waves were incident with different still water levels. When using the present wave dissipating blocks, the wave height transmission coefficient showed an increasing trend, as the still water level or incident significant wave height was increased. It was also confirmed that as the block arrangement density was decreased, the number of the fallen blocks increased, leading to the larger wave height transmission coefficient.

When the still water level is moderate, namely the HWL, the number of the fallen blocks was the largest, because the wave breaking often occurred just in front of the breakwater, without much energy decay before hitting the breakwater. Moreover, the overflow was the most effective to fall the blocks, owing to the adequate water depth over the breakwater, not too deep as with the HHWL. Therefore, block mound breakwaters should be designed considering both the block characteristics depending on block shape and arrangement density, and possible water depths where the breakwaters will be installed.

Second, we carried out the hydraulic experiments in which a long wave was incident. When the incident wave height is large, the entire breakwater was slightly lifted and shifted toward the shore, weakening the meshing of the blocks. The overflow that lasted for a long time fell many of the blocks at the back of the breakwater. Thereafter, the pulling wave generated the offshore flow, lowering the water level in the breakwater toward offshore, and several gravels placed below the breakwater were carried toward offshore.

Third, we conducted the hydraulic experiments in which irregular waves and a long wave were continuously incident. When the first series of irregular waves, a long wave, and the second series of irregular waves are continuously incident in this order, the first irregular wave train with a large significant wave height shifted several blocks, and the subsequent long wave dropped these shifted blocks, displacing the blocks around them. Then, the second irregular wave train dropped many of the displaced blocks. This suggests that when block displacements accumulate owing to one or several severe storms, the blocks may easily be slid down by harbor oscillations and swells caused by a subsequent storm.

Finally, we performed the vertically two-dimensional numerical calculations to obtain both the wave pressure and velocity vectors around the permeable detached breakwater. It turned out from the numerical results that the causes of the block sliding at the top behind the breakwater in the hydraulic experiments were the strong overflow and negative wave pressure. When the long wave struck the breakwater, a large-scale vortex was created near the seabed in front of the breakwater. The vortex stretched offshore and remained during the pushing wave. Even with a large incident long wave, when the wave breaking occurs offshore from the breakwater and the energy decay is large before the wave hit the breakwater, the absolute value of the negative wave pressure generated at the top behind the breakwater decreased. Based on both the numerical and experimental results, when a large positive wave pressure is generated behind the breakwater after a negative wave pressure without a large absolute value, the number of fallen blocks will reduce.

Conversely, when the short regular waves with a large wave height cause overtopping, the negative wave pressure frequently appeared behind the breakwater, although the duration of each overflow was short. This is consistent with the experimental results for the incident irregular waves with a large significant wave height, where the blocks at the back of the breakwater gradually shifted, loosening their engagement.

The numerical analysis revealed that the incidence of a long-period wave can generate a large-scale vortex in front of detached breakwaters and increase overflows leading to block sliding. Future work is required to consider a method that reduces the effect of such a vortex in three dimensions. Furthermore, it is important to organize the actual events to examine the response of blocks in the cases where waves with different periods are continuously incident.

7. Acknowledgments

Sincere gratitude is extended to Mr. Kentaro Kakiuchi of Penta-Ocean Construction Co., Ltd., and Mr. Kosuke Shimonishi of Tekken Corporation. They contributed to both the hydraulic experiments and numerical calculations when they were student members of our laboratory. I also express my gratitude to Mr. Kazuo Nakamura, a former technical staff member of Kagoshima University, who assisted in conducting the experiments.

8. References

[1] Uda T, Yabusaki Y, Murakami Y, Mizuno M. Nationwide actual situation of irregular block scattering of breakwaters in Japan. Proceedings of Japanese Conference on Coastal Engineering, JSCE. 1986; 33: 417-421. http://library.jsce.or.jp/jsce/open/00008/1986/33-0417.pdf.

[2] Matsutomi H, Sugisaki N. Movements of deformed concrete blocks forming detached breakwaters on Akita southern coast. Annual Journal on Coastal Engineering, JSCE. 1998; 45: 826-830 (in Japanese). http://library.jsce.or.jp/jsce/open/00008/1998/45-0826.pdf.

[3] Takayama T, Ikeda N. Wave transformation behind a broad submerged breakwater and effects of the breakwater on wave over-topping. Report of the Port and Harbour Research Institute. 1988; 27(4): 63-92 (in Japanese). https://www.pari.go.jp/search-pdf/vol027-no04-02.pdf.

[4] Nakayama A. An experimental study on hydraulic characteristics and stability of artificial barrier reef (2). Technical Report N.R.I.F.E. Aquaculture and Fishing Port. 1994; 16: 35-45.

[5] Kimura K, Shimizu Y, Taya T, Yamamoto Y, Doi Y, Hanzawa M. Characteristics of deformation and wave transmission for wide submerged breakwater with armor blocks. Annual Journal on Coastal Engineering, JSCE. 2002; 49: 816-820 (in Japanese). http://library.jsce.or.jp/jsce/open/00008/2002/49-0816.pdf.

[6] Medina J R, Hudspeth R T, Fassardi C. Breakwater armor damage due to wave groups. Journal on Waterway, Port, Coastal and Ocean Engineering. 1994; 120: 179-198.

[7] Iwagaki Y, Mase H, Kita N. Irregular wave simulation considering wave groups. Proceedings of Japanese Conference on Coastal Engineering, JSCE. 1982; 29: 55-59 (in Japanese). http://library.jsce.or.jp/jsce/open/00008/1982/29-0055.pdf.

[8] Itoh K, Higuchi Y, Toue T, Katsui H. DEM simulation of submerged breakwater deformation in consideration for randomness of rubbles. Annual Journal on Coastal Engineering, JSCE. 2001; 48: 806-810 (in Japanese). http://library.jsce.or.jp/jsce/open/00008/2001/48-0806.pdf.

[9] Maeno S, Ogawa M, Bierawski L G. Modeling submerged breakwater using VOF-DEM-FEM. Annual Journal on Coastal Engineering, JSCE 2006; 53: 886-890 (in Japanese). http://library.jsce.or.jp/jsce/open/00008/2006/53-0886.pdf.

[10] Araki S, Deguchi I. Numerical simulation on displacement of armor block on submerged breakwater with 3-dimensional DEM. Proceedings of the 21st International Offshore and Polar Engineering Conference. 2011; 3: 1152-1157.

[11] Milthaler F F M, Pavlidis D, Xiang J, Latham J-P, Pain C C, Vire A, Piggott M D, Farrell P E. The immersed body method combined with mesh adaptivity for fluid-solid coupling. In: Coastal Structures 2011, Takahashi S, Isobe M, Kobayashi N, Shimosako K. Eds. World Scientific. 2013. p. 277-283. https://doi.org/10.1142/9789814412216_0024.

[12] Campos Á, Castillo C, Molina-Sanchez R. Damage in rubble mound breakwaters. Part I: Historical Review of damage models. Journal of Marine Science and Engineering. 2020, 8(5); 317: 26 pages. https://doi.org/10.3390/jmse8050317.

[13] Campos Á, Molina-Sanchez R, Castillo C. Damage in rubble mound breakwaters. Part II: Review of the definition, parameterization, and measurement of damage. Journal of Marine Science and Engineering. 2020; 8(5): 306: 20 pages. https://doi.org/10.3390/jmse8050306.

[14] Goda Y, Yoshida H, Hachisuka K, Kuroki K. Derivation of new formulas for wave transmission coefficient of low-crested structures. ECOH/YG Technical Report. 2008; 9: 20 pages (in Japanese). https://www.ecoh.co.jp/tech/techlist/pdf/ECOHNo.9.pdf.

[15] Tomasicchio G R, D'Alessandro F. Wave energy transmission through and over low crested breakwaters. Journal on Coastal Research. 2013; Special Issue 65: 6 pages. https://www.jstor.org/stable/26482002.

[16] Kunimitsu M. An Example of analysis about damage of concrete block-type offshore breakwater. Journal of JSIDRE. 2004; 72-11: 961-964 (in Japanese). https://www.jstage.jst.go.jp/article/jjsidre1965/72/11/72_11_961/_pdf.
[17] Mase H, Yasuda T, Reis M T, Karunarathna H, Yang J-A. Stability formula and failure probability analysis of wave dissipating blocks considering wave breaking. Journal of Ocean Engineering and Marine Energy. 2015; 1: 45-54. https://doi.org/10.1007/s40722-014-0004-0.
[18] Ryu C, Kang Y, Kim J. Optimal design of rubble mound structures under the irregular wave. In: Coastal Engineering 1992, Edge B L, Ed. 1993. p. 1503-1516.
[19] Shimosako K, Osaki N, Nakano F. Reliability design of composite breakwaters based on sliding distance. Report of PARI. 2006; 45(3): 3-23 (in Japanese). https://www.pari.go.jp/search-pdf/vol045-no03-01.pdf.
[20] Tsujio D, Yasuda T. Optimum design for breakwaters covered with wave dissipating blocks considering life cycle cost. Journal of JSCE, Ser. B2 (Coastal Engineering). 2009; 65(1): 916-920. http://library.jsce.or.jp/jsce/open/00008/2009/56-0916.pdf.
[21] Uda T, Noshi Y, Hoshigami Y. Improvement of design criteria of detached breakwater, Journal of JSCE, Ser. B3 (Ocean Engineering). 2011; 67(2): I_1087-I_1092. https://doi.org/10.2208/jscejoe.67.I_1087.
[22] Lemos R, Santos J A, Fortes C J. Rubble mound breakwater damage assessment through stereo photogrammetry in physical scale laboratory tests. Ribagua. 2017; 4: 84-98. https://doi.org/10.1080/23863781.2017.1381455.
[23] De Almeida E, van Gent M R A, Hofland B. Damage characterization of rock slopes. Journal of Marine Science and Engineering. 2019; 7(10): 15 pages. https://doi.org/10.3390/jmse7010010.
[24] Takahashi S, Hanzawa M, Sugiura S, Shimosako K, van der Meer J. Performance design of maritime structures and its application to armor stones and blocks of breakwaters. In: Coastal Structures 2003, Melby J A. 2004. p. 14-26.
[25] Isobe M. Innovation for resilient coastal structures to reduce tsunami disaster. Journal of Disaster Research. 2016; 11: 1212-1220. https://doi.org/10.20965/jdr.2016.p1212.
[26] Kotake Y, Isobe M. Experimental study on pressure distribution along landward slope of coastal dike due to tsunami overflow. Journal of JSCE, Ser. B2 (Coastal Engineering). 2012; 68: 891-895 (in Japanese). https://www.jstage.jst.go.jp/article/kaigan/68/2/68_I_891/_pdf.
[27] Mikami T, Matsuba S, Shibayama T. Fluid motion around coastal dyke due to overflowing tsunami. Journal of JSCE, Ser. B2 (Coastal Engineering). 2013; 69(2): I_991-I_995 (in Japanese). https://www.jstage.jst.go.jp/article/kaigan/69/2/69_I_991/_pdf/-char/ja.
[28] Esteban M, Jayaratne R, Mikami T, Morikubo I, Shibayama T, Thao N D, Ohira K, Ohtani A, Mizuno Y, Kinoshita M, Matsuba S. Stability of breakwater armor units against tsunami attacks. Journal of Waterway, Port, Coastal and Ocean Engineering. 2014; 140: 188-198. https://ascelibrary.org/doi/epdf/10.1061/%28ASCE%29WW.1943-5460.0000227.
[29] Kato F, Suwa Y, Hatogai S, Fujita K. A study on structures of coastal dike that persist disaster mitigation effects against tsunami overflow. Journal of JSCE, Ser. B2 (Coastal Engineering). 2014; 70(1): 31-49 (in Japanese). https://doi.org/10.2208/kaigan.70.31.
[30] Honda T, Omata T, Oda Y, Ito K. Hydraulic physical experiments about local pressure on coastal dikes induced by tsunami overflow. Journal of JSCE, Ser. B3 (Ocean Engineering). 2016; 72(2): I_539-I_544 (in Japanese).
[31] Hanzawa M, Matsumoto A, Tanaka H. Stability of wave-dissipating concrete blocks of detached breakwaters against tsunami. In: Coastal Engineering 2012, Lynett P, Ed. 2013. p. 412-423.
[32] Nakamura T, Nezasa Y, Mizutani N, Kotake Y. Local scouring behind a coastal dike due to tsunami overflow and its countermeasures. Japanese Journal of Multiphase Flow. 2015; 29(2): 132-140 (in Japanese). https://doi.org/10.3811/jjmf.29.132.
[33] Ikari H, Harada E, Gotoh H. Particle-based simulation of detaching process of armor block from the top of coastal levee due to tsunami overtopping flow. Journal of JSCE, Ser. B1 (Hydraulic Engineering). 2018; 74(4): I_787-I_792 (in Japanese). https://doi.org/10.2208/jscejhe.74.I_787.
[34] Yamamoto T, Yasuda T. Numerical analysis about movement of tsunami boulder and storm boulder with SPH method. Journal of JSCE, Ser. B2 (Coastal Engineering). 2019; 75(2): I_433-I_438 (in Japanese). https://doi.org/10.2208/kaigan.75.I_433.
[35] Mitsui J, Kubota S, Matsumoto A. Trial simulation for movement of wave dissipating blocks using SPH method. Journal of JSCE, Ser. B2 (Coastal Engineering). 2020; 76(2): I_823-I_828 (in Japanese). https://doi.org/10.2208/kaigan.76.2_I_823.
[36] Ishikawa M, Kozuki Y, Yamanaka R, Okubo Y. Numerical analysis on robustness of streamlined coastal dikes in the tsunami overflow. Journal of JSCE, Ser. B3 (Ocean Engineering). 2014; 70(2): I_372-I_377 (in Japanese). https://doi.org/10.2208/jscejoe.70.I_372.

[37] Matsushima K, Mohri Y, Oogushi K, Tatsuoka F, Kiri H. Structural defects of cover-block type coastal dikes against tsunami bore and effective counter-measure. Journal of JSCE, Ser. B2. 2014; 70(2): I_986-I_990 (in Japanese). https://doi.org/10.2208/kaigan.70.I_986.
[38] Sakakiyama T. Stability formula for armor units against tsunami on rubble mound breakwater. Nuclear Risk Research Center Report, CRIEPI. 2015; O15001: 28 pages (in Japanese).
[39] Sogabe T, Ito S, Asakawa A, Nishida Y. Causes of damage to the block mound detached breakwater. Journal of Coastal Engineering, JSCE. 1982; 29: 423-427 (in Japanese). http://library.jsce.or.jp/jsce/open/00008/1982/29-0423.pdf.
[40] Nakaza E, Hino M. Reef-zone disaster caused by bore-like surf beat. Coastal Engineering in Japan. 1990; 33(1): 49-61. https://doi.org/10.1080/05785634.1990.11924522.
[41] Iwase H, Kato H, Suzuyama K, Inoue M. Damage from long swell to coastal protection facilities in a fishing port area and its effect on design offshore waves. Journal of JSCE, Ser. B2 (Coastal Engineering). 2021; 77(2): I_817-I_822.
[42] Kakinuma T. Long-wave generation due to atmospheric-pressure variation and harbor oscillation in harbors of various shapes and countermeasures against meteotsunamis. In: Natural Hazards. Tiefenbacher J P, Ed. IntechOpen. 2019. p. 81-109. https://doi.org/10.5772/intechopen.85483.
[43] Klein Breteler M, Provoost Y, 't Hart R. Stability of block revetments on low crested breakwaters. In: Coastal Structures 2011, Takahashi S, Isobe M, Kobayashi N, Shimosako K. World Scientific. 2013. p. 800-811.
[44] Arikawa T, Yamada H, Akiyama M. Examination of applicability of tsunami wave force in three-dimensional numerical wave tank. Annual Journal of Coastal Engineering, JSCE. 2005; 52: 46-50 (in Japanese). http://library.jsce.or.jp/jsce/open/00008/2005/52-0046.pdf.
[45] Coastal Development Institute of Technology. CADMAS-SURF/3D Research and Development of Numerical Wave Tank, CDIT Library Vol. 39, 2010. 235p. (in Japanese).
[46] Medina J R, Gómez-Martín M E, Corredor A. Influence of armour unit placement on armour porosity and hydraulic stability. In: Coastal Engineering 2010, Lynett P, Ed. 2013. p. 3072-3083. https://doi.org/10.9753/icce.v32.structures.41.
[47] Kakinuma T, Tomita T. Development of storm surge and tsunami simulator in oceans and coastal areas. In: Coastal Engineering 2004, Smith J M, Ed. 2005. p. 1552-1564. https://doi.org/10.1142/9789812701916_0124.